Three-dimensional numerical simulations of mantle flow beneath mid-ocean ridges

Christina Morency, M.P. Doin, C. Dumoulin

Three-dimensional numerical simulations of mantle flow beneath mid-ocean ridges

C. Morency[1]
Géosciences Rennes, Campus de Beaulieu, Rennes, France

M.-P. Doin
Laboratoire de Géologie, Ecole Normale Supérieure, Paris, France

C. Dumoulin
Laboratoire de Planétologie et Géodynamique, Université de Nantes, Nantes, France

Received 27 September 2004; revised 13 July 2005; accepted 22 August 2005; published 18 November 2005.

[1] We perform three-dimensional (3-D) numerical simulations of an oceanic lithosphere cooling above a convective mantle to investigate mantle flow geometry and its associated lithospheric features. A constant horizontal velocity (half spreading velocity) of 2 (or 4) cm/yr is applied at the box surface to mimic plate motion. In all cases, because of the temperature-dependent viscosity, a rigid conductive lithosphere cools progressively beneath the two plates separated by the ridge. After 16–40 Ma, cold downgoing instabilities develop at the base of the lithosphere. Small-scale convection is then superimposed on the large-scale circulation. It produces, and then interacts with, a slowly evolving short-wavelength isotherms topography at the base of the lithosphere. The influence of the imposed ridge geometry on the mantle flow appears by comparison of simulations with case A, a linear ridge perpendicular to the plate motion; case B, a linear ridge strongly oblique to the plate motion; and case C, a ridge with transform faults along the spreading center with a mean orientation strongly oblique to the plate motion. All simulations reveal complex interaction between the isotherm topography within the base of the lithosphere, the small-scale flow generated at or just below the base of the lithosphere, and the large-scale flow dominating in the mantle below. The large-scale flow appears always controlled by the mean ridge axis direction and thus may be oblique to the imposed plate motion direction. It is enhanced by the instabilities development. We argue that the large-scale flow orientation results from the interaction with the small-scale velocity field which flows down the isotherm topography at the base of the lithosphere. The latter is either inherited (lithospheric cooling, transform faults) or develops as boundary layer instabilities.

Citation: Morency, C., M.-P. Doin, and C. Dumoulin (2005), Three-dimensional numerical simulations of mantle flow beneath mid-ocean ridges, *J. Geophys. Res.*, *110*, B11407, doi:10.1029/2004JB003454.

1. Introduction

[2] The oceanic lithosphere plays an important role in the heat transfer on Earth. However, its thermal structure strongly depends on the convective flow pattern at its base, which has not yet been fully studied.

[3] As the oceanic lithosphere cools away from the ridge axis, a rigid conductive upper boundary layer forms. For many years, a purely conductive half-space cooling model was used to explain the cooling of the oceanic lithosphere and the subsidence of the seafloor topography [*Turcotte and Oxburgh*, 1967; *Parsons and Sclater*, 1977]. This model fits the data at young ages, but it does not explain the flattening of the oceanic floor and of the surface heat flow at old ages. Departure from the half-space cooling model is often thought to result from the interaction with the convective upper mantle. As shown, for example, by *Davaille and Jaupart* [1993], *Dumoulin et al.* [2001], *Korenaga and Jordan* [2003], and *Huang et al.* [2003], when the upper thermal boundary layer of a convecting system cools, its lower part becomes unstable: Small-scale instabilities appear at the bottom of the stiff plate once a critical age of the thermal boundary layer is reached. This small-scale convection (SSC) located at the base of the lithosphere is superimposed to the large-scale convection linked to plate tectonics. Cold blobs sink into the convective mantle and

[1]Now at Department of Oceanography, Dalhousie University, Halifax, Nova Scotia, Canada.

0148-0227/05/2004JB003454$09.00

are replaced by hot material, transferring heat upward and limiting the upper thermal boundary layer cooling. This process has been invoked to explain the flattening of the seafloor subsidence, of the heat flow, and of the geoid, observed at old ages [*Parsons and McKenzie*, 1978; *Stein and Stein*, 1992; *Doin and Fleitout*, 2000], and the rapid decrease of geoid jumps across transform faults as a function of age [*Sandwell and Schubert*, 1982; *Cazenave et al.*, 1983; *Driscoll and Parsons*, 1988; *Freedman and Parsons*, 1990]. A recent tomographic study, based on surface wave dispersion measurements beneath the Pacific Ocean, provides evidence for a lithosphere reheating from 70 Ma with respect to a purely conductive cooling, that could result from thermal boundary layer instability development [*Ritzwoller et al.*, 2004].

[4] If the physics of SSC beneath a rigid lid is well understood and parameterized [*Davaille and Jaupart*, 1993; *Dumoulin et al.*, 1999; *Solomatov and Moresi*, 2000], its observation on Earth is still under debate. [*Haxby and Weissel*, 1986] report short-wavelength geoid undulations (wavelengths between 150 and 500 km) in the Pacific Ocean. These lineations in the direction of absolute plate motion may represent an indirect observational evidence of SSC beneath the oceanic lithosphere. *Morgan and Parmentier* [1995] also linked mantle circulation at the base of the oceanic lithosphere to geoid lineations observed in the southwest Indian Ocean and in the northern Mid-Atlantic Ocean. Using a two-dimensional (2-D) model of convection beneath young oceanic lithosphere with a viscosity depending strongly on temperature, *Buck and Parmentier* [1986] show that SSC can produce the magnitude of the short-wavelength gravity anomalies observed by *Haxby and Weissel* [1986].

[5] Seismic anisotropy can also be a useful tool to investigate the mantle flow geometry beneath the oceanic lithosphere. In first approximation, seismic anisotropy results from the preferred orientation of olivine crystals deformed within the upper mantle flow. Global 3-D anisotropic models in the uppermost mantle cannot be entirely explained by the large-scale mantle shear produced by tectonic plate motions [*Becker et al.*, 2003]. *Ekström and Dziewonski* [1998] and *Montagner* [2002] consider the additional contribution of SSC or of a complex pattern of horizontal flow generated by the injection of material into the asthenosphere by mantle plume. Anisotropy study in the Indian Ocean upper mantle also shows that in the uppermost 100 km the pattern of fast velocity directions is complex and does not correlate simply with plate motions [*Lévêque et al.*, 1998].

[6] The 3-D mantle flow geometry beneath a moving plate has been investigated by *Richter and Parsons* [1975] using 3-D isoviscous experimental models. They show that the large-scale shear generated by the moving upper surface destroys the original convective pattern and promotes a set of rolls with axes lining up in the direction of the large-scale flow (longitudinal rolls or "Richter rolls"). These rolls full the whole convecting box and retain an aspect ratio of about one. The time necessary for the longitudinal rolls development strongly varies (40–200 Ma) depending on the Rayleigh number and on the plate velocity. However, the use of an isoviscous fluid in this experimental setup precludes the formation of a rigid and conductive cooling lithosphere. When the viscosity depends strongly on temperature, small-scale convection takes the form of thermal boundary layer instabilities, affecting only a thin sublayer at the base of the lithosphere, and whose onset is delayed with respect to the ridge [e.g., *Davaille and Jaupart*, 1993; *Korenaga and Jordan*, 2003; *Huang et al.*, 2003; *Dumoulin et al.*, 2005]. Some 3-D transient cooling numerical simulations, with a large viscosity contrast between two isoviscous stratified layers, show that instabilities occur preferentially below active transform segments and may then become oblique to the plate motion direction [*Rabinowicz et al.*, 1993].

[7] The dependence of geometry, wavelength, and onset time of longitudinal rolls (Richter rolls) on model parameters has not yet been fully explored. Simulations performed by *Marquart* [2001] with different Rayleigh numbers and plate velocities show that they depend on the relative amplitude between the imposed surface velocity and the maximum horizontal velocity in the convective mantle, and on the chosen rheology. In the case of a temperature- and pressure-dependent viscosity, *Marquart* [2001] found that rolls are limited to the low viscosity layer (asthenosphere), whereas, in the isoviscous case, they fill the whole upper mantle. By comparing 2-D and 3-D simulations performed with a temperature-dependent Newtonian viscosity, *van Hunen et al.* [2003] show that scaling laws for the SSC onset time obtained from previous 2-D studies [*Huang et al.*, 2003] are also for 3-D models to the first order. In their simulations, SSC, deriving from the destabilization of the upper thermal boundary layer, displays roll structures parallel to plate motion.

[8] In this study, we investigate the flow pattern in the case of a linear ridge axis perpendicular to the plate motion, a linear ridge axis strongly oblique to the plate motion, and in the case of a ridge with transform faults along the spreading center with a mean ridge axis strongly oblique to the plate motion. We use a Newtonian rheology with a viscosity depending strongly on temperature, following an Arrhenius law. We raise the question of the influence of transform faults along the ridge axis on the flow pattern.

2. Model Setup

[9] We use a 3-D numerical code [*Albers*, 2000] based on a finite volume discretization in the primitive variable formulation (temperature, pressure, stress, and velocity). This code solves, by a multigrid method, the conservation equations for mass, momentum (with infinite Prandtl number), and energy, in the Boussinesq approximation:

$$\nabla \cdot \mathbf{u} = 0 \tag{1}$$

$$-\nabla P + \nabla \cdot \left[\nu\left(\nabla \mathbf{u} + \nabla^T \mathbf{u}\right)\right] + \rho_0[1 - \alpha(T - T_0)]\mathbf{g} = 0 \tag{2}$$

$$\rho_0 Cp(\partial T/\partial t + \mathbf{u} \cdot \nabla T) - k\nabla^2 T - Q = 0 \tag{3}$$

where T, $\mathbf{u}$, ν, and P are the temperature, the velocity vector, the viscosity, and the pressure, respectively, and where other symbols are defined in Table 1 (bold indicates vectors).

Table 1. Parameters

Variables	Symbols	Values
Temperature difference	ΔT	1400°C
Box height	H	400 km
Preexponential constant	A	1.045×10^{11} Pa s
Activation energy	E_a	219 kJ mol^{-1}
Thermal expansion coefficient	α	3×10^{-5} K^{-1}
Thermal diffusivity	κ	0.8×10^{-6} m^2 s^{-1}
Thermal conductivity	k	3.3 W m^{-1} K^{-1}
Density	ρ_0	3300 kg m^{-3}
Heat capacity	C_p	1.25 kJ kg^{-1} K^{-1}
Plate velocity	u_0	2 and 4 cm yr^{-1}
Radiogenic heat production	Q	117.5 μW m^{-3}
Gas constant	R	8.32 J mol^{-1} K^{-1}
Gravity acceleration	g	9.81 m s^{-2}

Adiabatic and shear heating in the energy equation (3) are neglected. The robustness of the code has been successfully tested by comparing its results with benchmark experiments that have been published for 2-D [*Blankenbach et al.*, 1989] and 3-D [*Busse et al.*, 1993] convective problems with infinite Prandtl number. The Rayleigh number is set to 4.2×10^7.

[10] The implemented rheology is a uniform Newtonian viscous behavior, following an Arrhenius law depending strongly on temperature:

$$\nu = A \exp\left(\frac{E_a}{RT}\right) \tag{4}$$

where T is the absolute temperature (other symbols and their values are defined in Table 1). This rheology results in the self-consistent formation of a rigid surface layer in convective simulations [*Morris and Canright*, 1984] that is equated with the lithosphere. With such a rheology, weak plate boundaries and plate motions do not appear as a result of the convective flow. As we are concerned here by the influence of the plate motion and geometry on the convective flow beneath the plate, we impose in our simulations lithospheric surface motion.

[11] We choose a simple two plates geometry diverging at a total velocity of $2 \times u_0$: a constant velocity of $\pm u_0$ (2 or 4 cm yr^{-1}) is applied at the box surface on each plate. Three ridge geometries have been tested (see Figure 1): Case A, a linear ridge perpendicular to the plate motion; case B, a linear ridge strongly oblique to the plate motion; and case C, a ridge with transform faults along the spreading center with a mean ridge orientation strongly oblique to the plate motion. We are aware that case B is not a realistic case on Earth, but it is useful to understand and to discuss the results of the other cases.

[12] Other boundary conditions are as follow (see Figure 2): Free slip closed boundary conditions are imposed at the front and back sides. The left and right boundaries are free slip open, with vanishing tangential viscous stresses and locally constant normal stress ($\partial v_x^2/\partial x^2 = \partial v_y/\partial x = \partial v_z/\partial x = \partial P/\partial x = 0$.) Finally, a no-slip open boundary condition is applied at the bottom, with vanishing tangential velocities and normal viscous stress ($v_x = v_y = \partial v_z/\partial z = \partial P/\partial z = 0$). Because of these boundary conditions the cooled old lithosphere disappears on the box right and left sides, and the return flow enters the box mainly by its base.

[13] The box is heated from within and the temperature at the box base is set to 1400°C. Therefore, in all simulations presented here, the material inflow within the box base has a fixed temperature, that is, because of internal heating, very slightly lower than the core flow temperature. As a result, the upwellings carry, in the present simulations, no positive buoyancy and are passive.

[14] To limit the influence of the boundary conditions on the convective cells evolution, we use an aspect ratio of $6 \times 3 \times 1$ when the surface velocity is equal to 2 cm yr^{-1}, and $12 \times 6 \times 1$ when the surface velocity is equal to 4 cm yr^{-1}. The box width, length, and depth for u_0 = 2 cm yr^{-1} are then 2400, 1200, and 400 km, respectively, and for u_0 = 4 cm yr^{-1}, 4800, 2400, and 400 km, respectively. The ratio between the horizontal box dimensions and the surface velocity is thus the same in both cases. The transform fault spacing and length is twice larger for

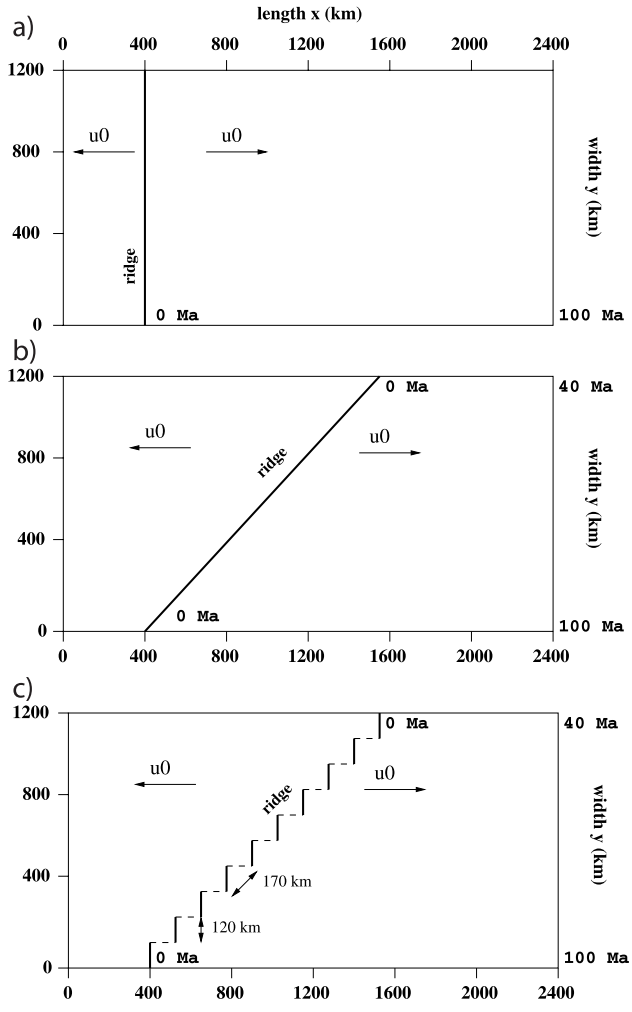

Figure 1. Schematic representation of the three studied ridge geometries, in the case of surface velocity equal to 2 cm yr^{-1}: (a) linear ridge perpendicular to the plate motion, (b) a linear ridge strongly oblique to the plate motion, and (c) ridge with transform faults along the spreading center with a mean ridge orientation strongly oblique to the plate motion.

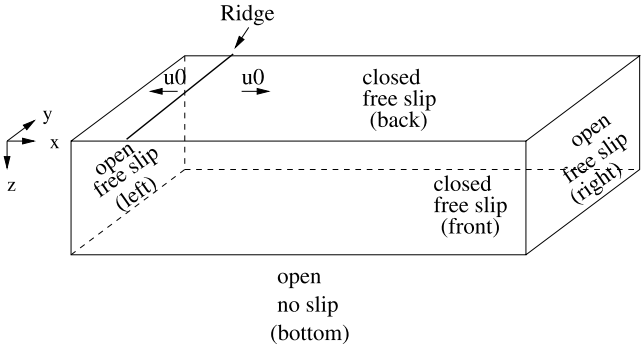

Figure 2. Simulation boundary conditions.

u_0 = 4 cm yr^{-1} than for u_0 = 2 cm yr^{-1}, such that both the age offset across transform faults and the mean ridge orientation are the same for the two surface velocities. For u_0 = 2 cm yr^{-1}, the numerical mesh is made of 144 × 72 × 24 regularly spaced points but is refined by a factor two in each directions in the upper half box. For u_0 = 4 cm yr^{-1}, the numerical mesh is made of 288 × 144 × 24 regularly spaced points.

[15] The initial thermal state in our experiments is a result of a convective simulation performed without surface motion until a statistically steady state is reached. The corresponding flow structure is polygonal (see Figure 3). The flow ascends in polygon centers and forms an irregular network of descending sheets. This is consistent with 3-D numerical simulations of mantle convection with temperature-dependent viscosity and rigid boundary conditions [*Christensen and Harder*, 1991; *Tackley*, 1993].

[16] In sections 3–5, we describe and discuss the 3-D mantle flow geometry and the thermal state obtained when surface plate motions are imposed. The simulation duration exceeds 100 Myr, which is the time necessary for a material point, initially located at the ridge, to cross the box entirely and to escape by its sides. After 100 Myr, all lithospheric material present in the box has been accreted at the ridge. Note that parameter values necessary for simulation scaling are displayed on Table 1.

3. Linear Ridge Perpendicular to the Plate Motion (Case A)

3.1. Flow Description at 100 Myr for a Surface Velocity of 2 cm yr^{-1}

[17] In the following, we first present results obtained in the case of a constant surface velocity of 2 cm yr^{-1}, after a simulation time of 100 Myr.

[18] The imposed diverging plate velocity results in the formation of a ridge axis from which the lithosphere cools with age by thermal conduction. This corresponds to a lithospheric thickness increase and to a decrease of the surface heat flow (Figure 4). At old ages, the surface heat flow and lithospheric thickness evolution flattens because heat is brought to the base of the lithosphere by the SSC. Parameter values and box scaling have been chosen in order to have surface heat flow and lithospheric thickness evolutions approximatively match the predictions of the plate or constant heat flow models, when adjusted to observations [e.g., *Parsons and Sclater*, 1977; *Stein and Stein*, 1992; *Doin and Fleitout*, 1996]. These choices will be discussed in section 6.5.

[19] The temperature isosurface at 1380°C is shown on Figure 5a. We clearly note the formation of downgoing instabilities affecting the base of the lithosphere, nearly parallel to the ridge axis. The flow and the temperature structure are two dimensional at young ages. A second series of downgoing instabilities appears later, 1250 km away from the ridge axis. It remains mostly perpendicular to the ridge axis along a 300 km wide swath. Further away

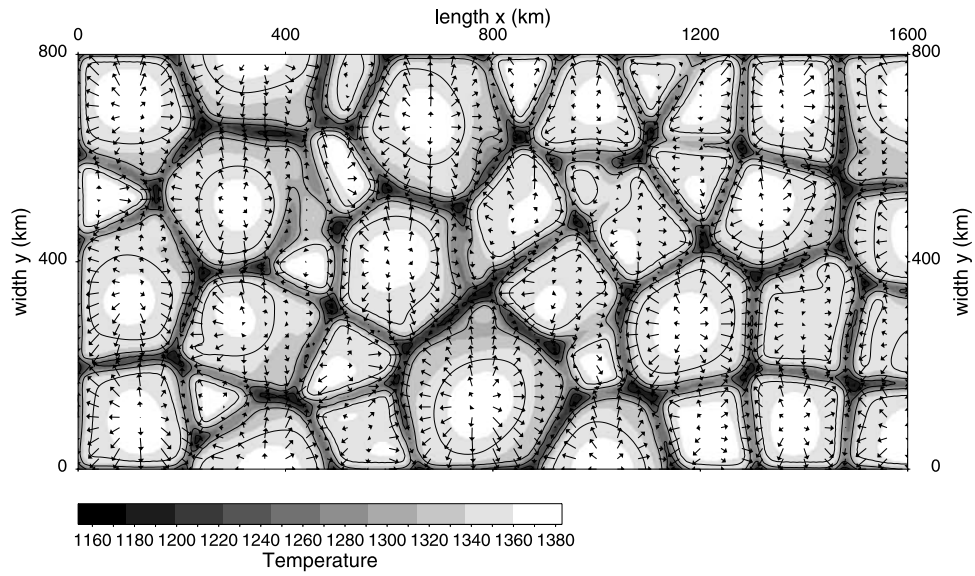

Figure 3. Initial temperature and horizontal velocity field on an horizontal plane at 104 km depth (mean value of the lithospheric depth). Maximum velocity is 2.7 cm yr^{-1}.

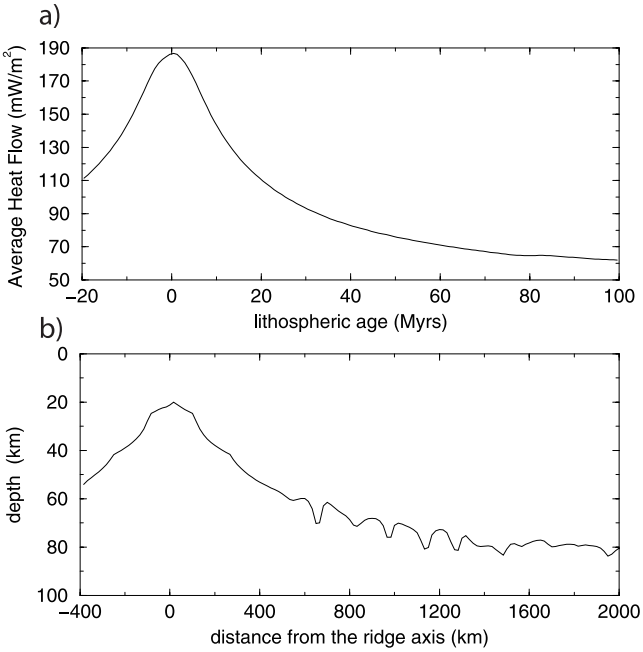

Figure 4. (a) Heat flow (average along the y direction) as a function of lithospheric age and (b) lithospheric thickness profile at y = 600 km. The lithospheric thickness is defined as the depth reached by the 1300°C isotherm.

from the ridge axis, at around 1600 km, an irregular small-scale flow pattern dominates.

[20] The first downgoing instability appears at about 640 km (32 Ma) from the ridge axis. This result is in good agreement with two dimensional scaling laws describing the onset of small-scale instabilities at the base of the lithosphere [*Huang et al.*, 2003; *Dumoulin et al.*, 2005]. Ridge-parallel downgoing instabilities are spaced every 150 km, whereas ridge-perpendicular downgoing instabilities are spaced every 110 km.

[21] Although the temperature structure presents small-scale perturbations, the flow in the mantle has mostly a large-scale structure and is globally oriented in the imposed plate motion direction. Note, however, that it flows at a faster pace than plate motion, especially as soon as the instabilities develop (Figure 6a). This mantle flow is therefore not simply the result of the shearing between the imposed horizontal velocity at top and bottom (u_0 and zero, respectively), but it is also driven by internal buoyancy forces. The "additional" large-scale flow thus dissipates the work of gravity forces acting on negatively buoyant boundary layer instabilities. In a cross section perpendicular to the plate motion, we note again that the main mantle flow structure occurs at a larger scale than the instability spacing (Figure 6b). However, in a small layer close to the base of the lithosphere, the flow appears at a smaller scale, looking more or less alike Richter rolls. This can be better visualized when we plot the horizontal velocity field in the unstable thermal boundary layer at the base of the lithosphere relative to plate motion (Figure 7). This flow is linked to the instability development and therefore presents a pattern at the same scale as temperature perturbations. It follows the lithosphere basal topography gradients. It goes faster than the plate downstream of the topography (close to the ridge or before an instability) and slows down upstream (after an instability).

3.2. Evolution With Simulation Time for a Surface Velocity of 2 cm yr^{-1}

[22] Even after the memory of the initial lithospheric structure is lost by advection across the left and right sides of the box (after 100 Myr), the small-scale instability pattern continues to slowly evolve with time. On Figure 5, the temperature isosurface at 1380°C is displayed for scaled simulation times of 100 (Figure 5a), 138 (Figure 5b), and 185 Myr (Figure 5c). We note that ridge-perpendicular instabilities develop through time at the expense of the irregular pattern (Figure 5b). This evolution is related to a joint change in the large-scale mantle flow, which presents at 185 Myr a forward horizontal motion extending to larger x than at 100 Myr (Figures 6a and 6c). This forward mantle shearing favors the small-scale instabilities alignment along plate motion direction. We also observe a competition between ridge-perpendicular and ridge-parallel instabilities (Figures 5b and 5c). Reflecting this competition, the three-dimensional small-scale flow associated to ridge-perpendicular instabilities, observed on Figure 6b at x = 2000 km at a simulation time of 100 Myr, is slowly replaced in the box center by a two dimensional flow (Figure 6d). Although ridge-perpendicular instabilities are known to develop preferentially in the presence of a shear flow [e.g., *Richter*, 1973], ridge-parallel instabilities here grow first. These instabilities are probably promoted because they share the symmetry (invariance along y axis) of the ridge axis and of the lithospheric cooling structure: A drip, uniform along y direction, develops when, at a given x, the lithospheric sublayer structure, also invariant along y, becomes unstable. These "frozen" instabilities are then advected with plate motion and new ridge-parallel instabilities are generated at the same distance from the ridge. They are eventually destroyed by the development of the intrinsically more stable ridge-perpendicular instabilities. The slowly building "V" shape formed by ridge-perpendicular instabilities suggests that the latter are favored by the free slip closed boundary conditions applied on the sides. We will focus on the influence of boundary conditions in section 6.

3.3. Flow Description for a Surface Velocity of 4 cm yr^{-1}

[23] Almost the same observations hold for a simulation performed using a constant surface velocity of 4 cm yr^{-1}. The onset time of the first instability, of about 40 Ma, is slightly greater than the onset time obtained in the previous case. There is again a competition between the development of ridge-parallel and ridge-perpendicular instabilities. However, for a surface velocity of 4 cm yr^{-1}, ridge-perpendicular instabilities take place at a younger lithospheric age and a lower simulation time than for u_0 = 2 cm yr^{-1}. They are already well developed at a simulation time of 100 Myr (Figure 8a). Ridge-parallel instabilities take slightly over ridge-perpendicular instabilities at 147 Myr, however, after 188 Myr, they have disappeared

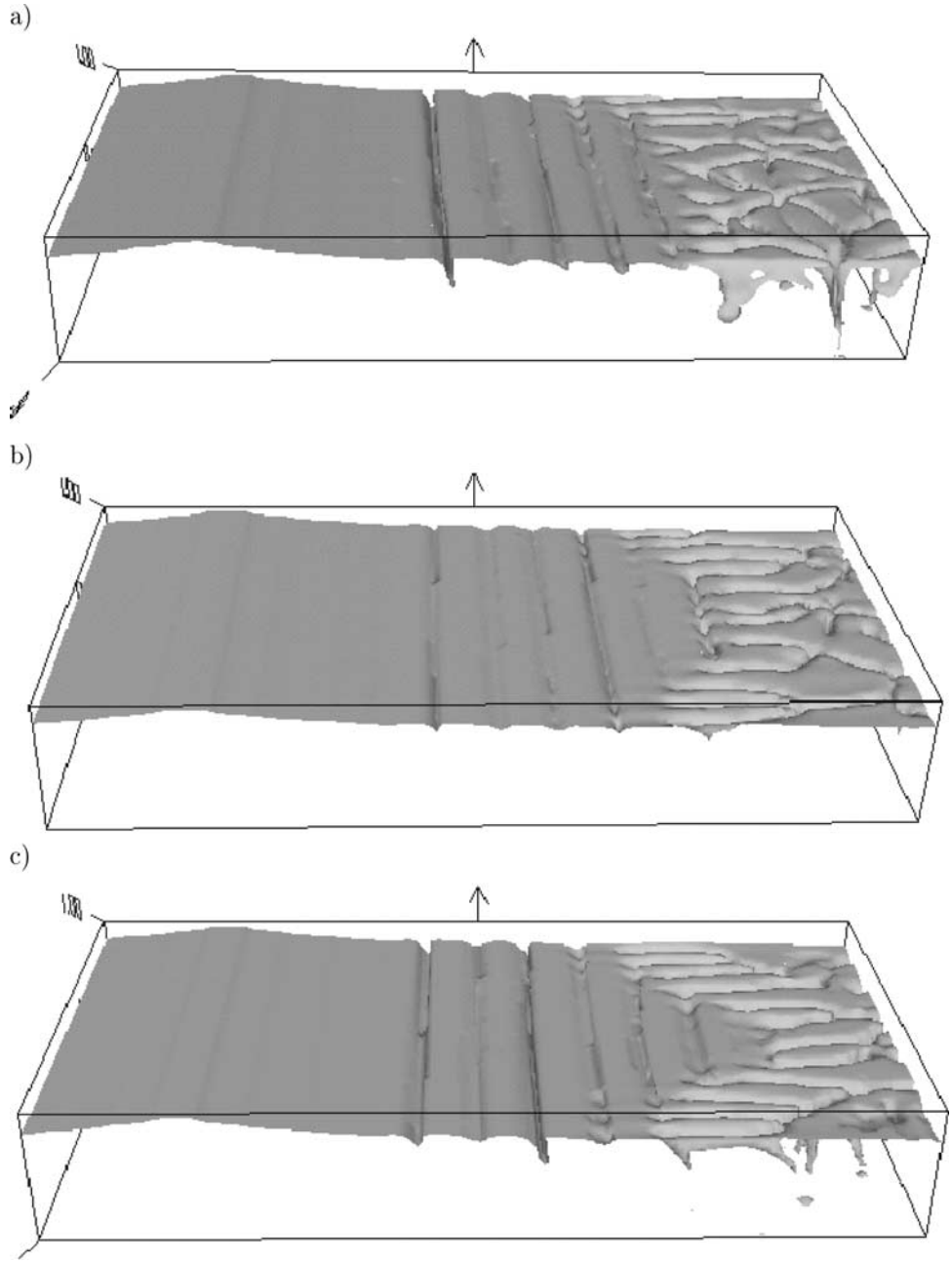

Figure 5. Simulation A temperature isosurface at 1380°C at scaled simulation times of (a) 100, (b) 138, and (c) 185 Myr and u_0 = 2 cm yr^{-1}.

and are replaced by ridge-perpendicular instabilities (Figure 8). The spacing between these ridge-perpendicular downgoing instabilities, of about 110 km (Figure 9), is very close to that obtained in the 2 cm yr^{-1} plate velocity case.

[24] As for a surface velocity of 2 cm yr^{-1}, the mantle flow presents mainly a large-scale pattern, mostly lined up with plate motion for $x < 4000$ km and producing a forward shearing as soon as instabilities develop. In a vertical cross section parallel to the ridge (and perpendicular to the main flow direction), we note again that the small-scale flow associated with thermal anomalies prevails at the lithosphere/asthenosphere boundary but is progressively replaced with depth by a larger-scale flow (Figure 9).

4. Linear Ridge Strongly Oblique to the Plate Motion (Case B)

4.1. Flow Description for a Surface Velocity of 2 cm yr^{-1}

[25] Downgoing instabilities appear 680 km away from the ridge axis (~34 Ma, close to the case with a linear ridge perpendicular to the plate motion). They develop first as ridge-parallel instabilities in the box center and as ridge-perpendicular instabilities on the box sides (Figure 10). As

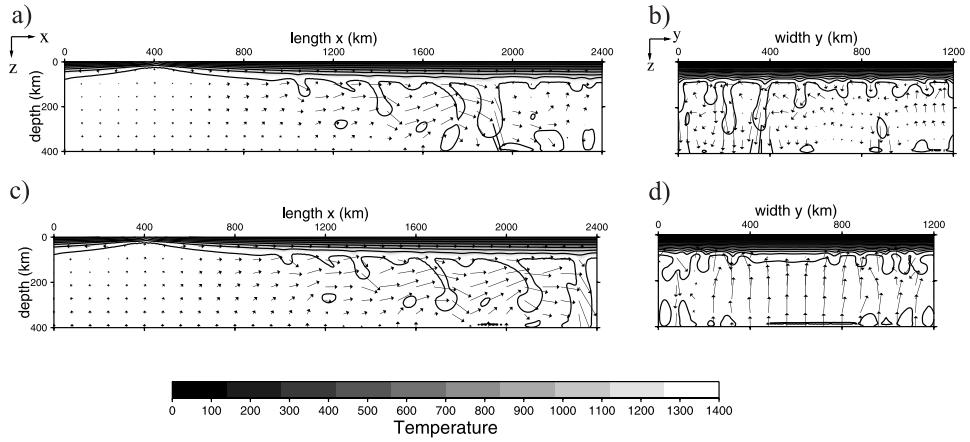

Figure 6. Results obtained for simulation A and u_0 = 2 cm yr^{-1}: Temperature and velocity fields are displayed on a vertical plane located (a) at y = 583 km from the box right side and (b) at x = 2000 km from the box front size, at a scaled simulation time of 100 Myr. (c) and (d) Same fields plotted at a scaled simulation time of 185 Myr. Maximum velocities are equal to 22.77 (Figure 6a), 12.40 (Figure 6b), 17.40 (Figure 6c), and 5.54 cm yr^{-1} (Figure 6d).

in previous simulations, ridge-perpendicular instabilities form a V shape pattern. At old ages, the instability pattern is irregular but disappears at the favor of ridge-perpendicular instabilities, when simulation time increases (Figure 11a). The competing development of ridge-perpendicular and ridge-parallel instabilities leads to a quasi static steady state (Figures 10 and 11a). The spacing between ridge-parallel and ridge-perpendicular instabilities is equal to 145 and 120 km, respectively, close to the previous cases.

[26] Shearing by plate motion here does not favor the development of instabilities parallel to plate motion. The stable instability orientation is controlled by the main mantle flow shearing, which is oriented perpendicular to the ridge and is oblique to plate motion (Figures 10 and 11a). Looking at the flow at the base of the lithosphere relative to plate motion, we see that it always follows the lithosphere topography, generated by downgoing instabilities or by lithospheric cooling. Thus the flow at the base of the lithosphere, controlled by the isotherm topography, is strongly oblique to the plate motion at young ages (Figure 10).

[27] Deeper in the mantle (Figure 11a), the flow has a large-scale structure. It is small and oriented parallel to the ridge next to the ridge, it then rotates parallel to plate

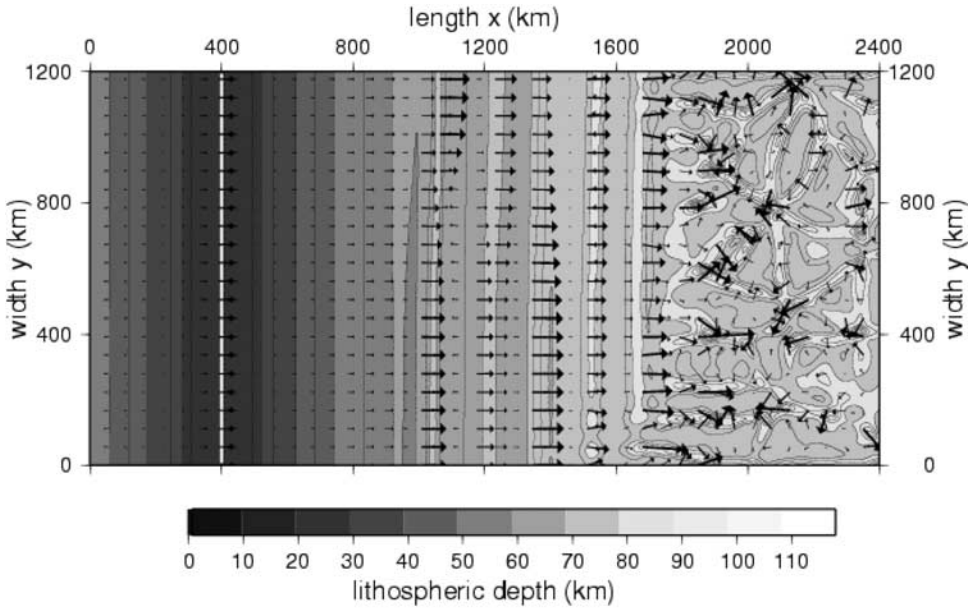

Figure 7. Horizontal velocity field (minus the plate velocity value of 2 cm yr^{-1}) displayed along the 1300°C isotherm. The gray scale represents the 1300°C isotherm depth. Scaled simulation time is 100 Myr.

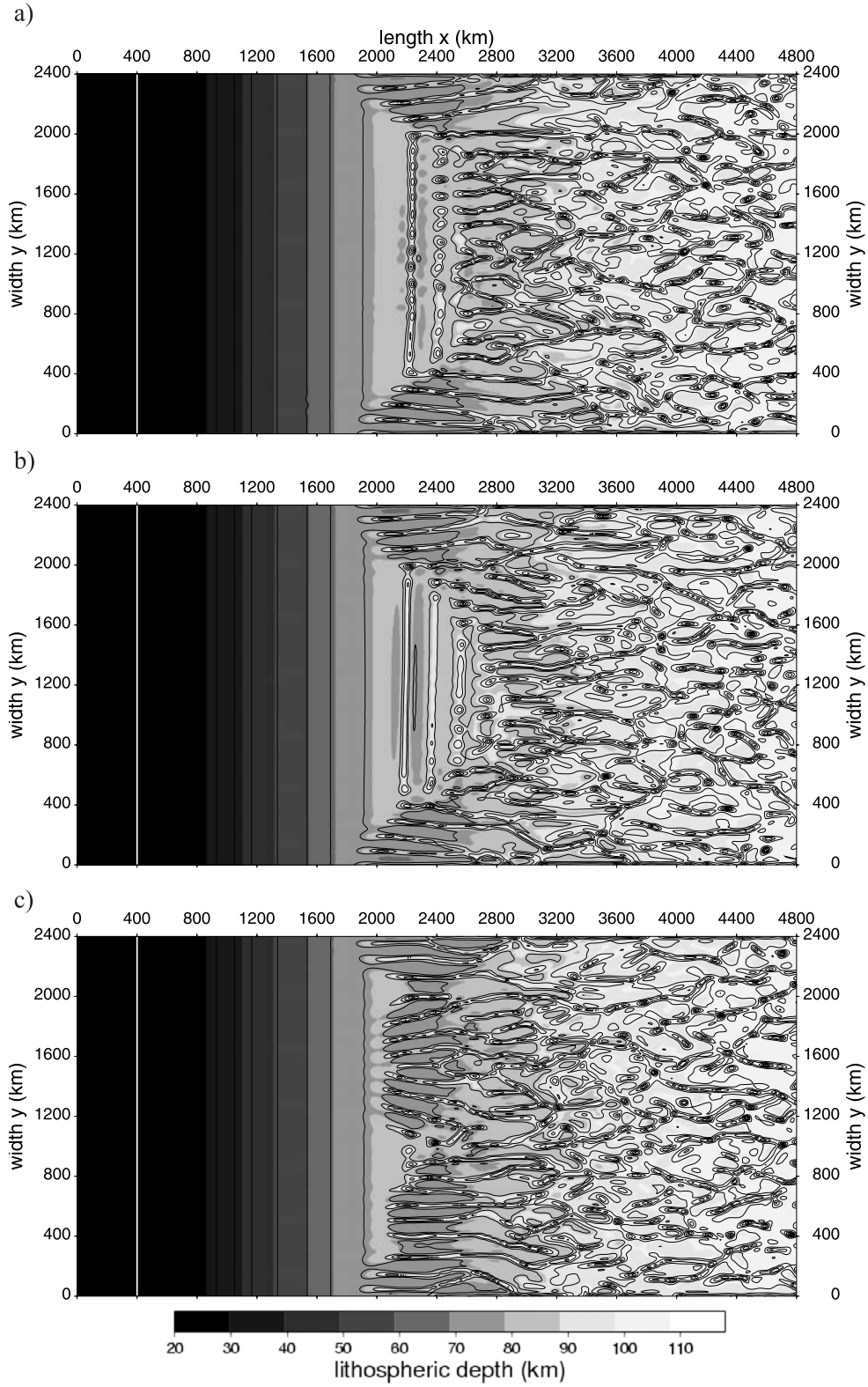

Figure 8. Results for simulation A with u_0 = 4 cm yr^{-1}: Lithospheric depth (evaluated at the 1300°C isotherm), at scaled simulation times of (a) 100, (b) 147, and (c) 188 Myr.

motion 200 km away from the ridge, and finally, as the instabilities develop (~400 km away from the ridge), the mantle flows faster than the imposed plate motion and rotates toward the ridge perpendicular orientation. To understand the origin of the large-scale flow, the passive flow due to plate motion was computed in the same conditions (Figure 11b). Passive entrainment by plate motion well explains the flow close to the ridge but does not display

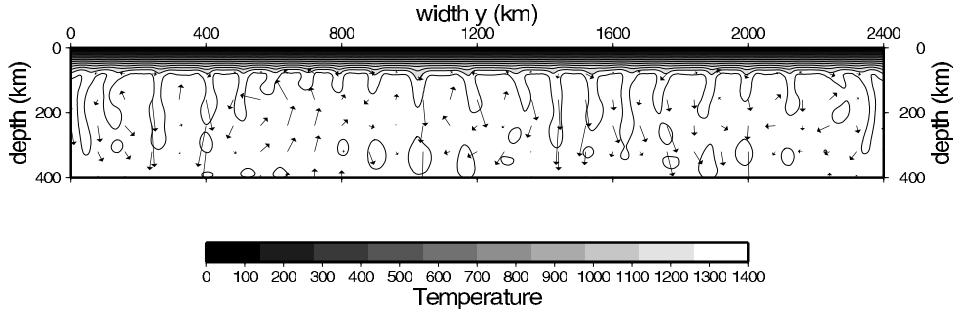

Figure 9. Results of simulation A with $u_0 = 4$ cm yr^{-1}: Temperature and velocity fields displayed on a vertical plane located at $x = 2400$ km at a scaled simulation time of 188 Myr. Maximum velocity is of 9.50 cm yr^{-1}.

the velocity increase and flow reorientation ~400 km away from the ridge. The additional mantle flow (not linked to the plate motion drag) is oriented perpendicularly to the ridge and must be generated by buoyancy forces, i.e., by the lithosphere boundary layer instabilities (we recall that upwelling here carries no positive buoyancy). In turn, the additional mantle flow influences the instability orientation.

4.2. Flow Description for a Surface Velocity of 4 cm yr^{-1}

[28] The instabilities and flow patterns, for a surface velocity of 4 cm yr^{-1}, present many similarities to the previous case with a lower plate velocity. Ridge-parallel instabilities develop preferentially in the middle of the box, whereas ridge-perpendicular instabilities form a V shape pattern, that seems to be triggered by box sides (Figure 12). Both series of downgoing instabilities compete each other, leading to a quasi static steady state. The spacing between ridge-parallel and ridge-perpendicular instabilities are equal to 175 and 145 km, respectively, slightly larger than in the previous case. However, here, the onset time of ridge-perpendicular and ridge-parallel instabilities differs, being approximatively 20 and 40 Ma, respectively.

[29] The flow at the base of the lithosphere follows the isotherm topography. The deeper mantle flow has again a large-scale structure. Close to the ridge, it presents the same characteristics as the passive flow due to plate motion, i.e., next to the ridge, a flow parallel to the ridge directed toward the acute angle between the ridge direction and the plate motion and 400 km away from the ridge, a progressive reorientation toward the plate motion. However, 1200 km away from the ridge, when instabilities develop at about 30 Ma, the flow velocity increases and rotates perpendicularly to the ridge axis (Figure 12). Finally, "ridge-perpendicular" instabilities line up with the mantle

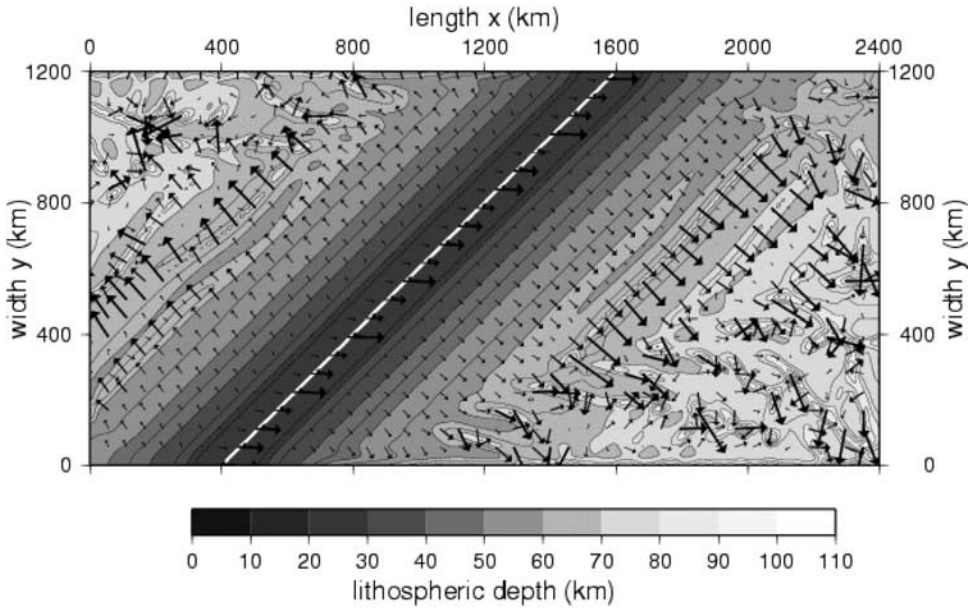

Figure 10. Results of simulation B with $u_0 = 2$ cm yr^{-1}: Horizontal velocity field (minus the plate velocity value of 2 cm yr^{-1}) displayed along the 1300°C isotherm. The gray scale represents the 1300°C isotherm depth. Scaled simulation time is 116 Myr.

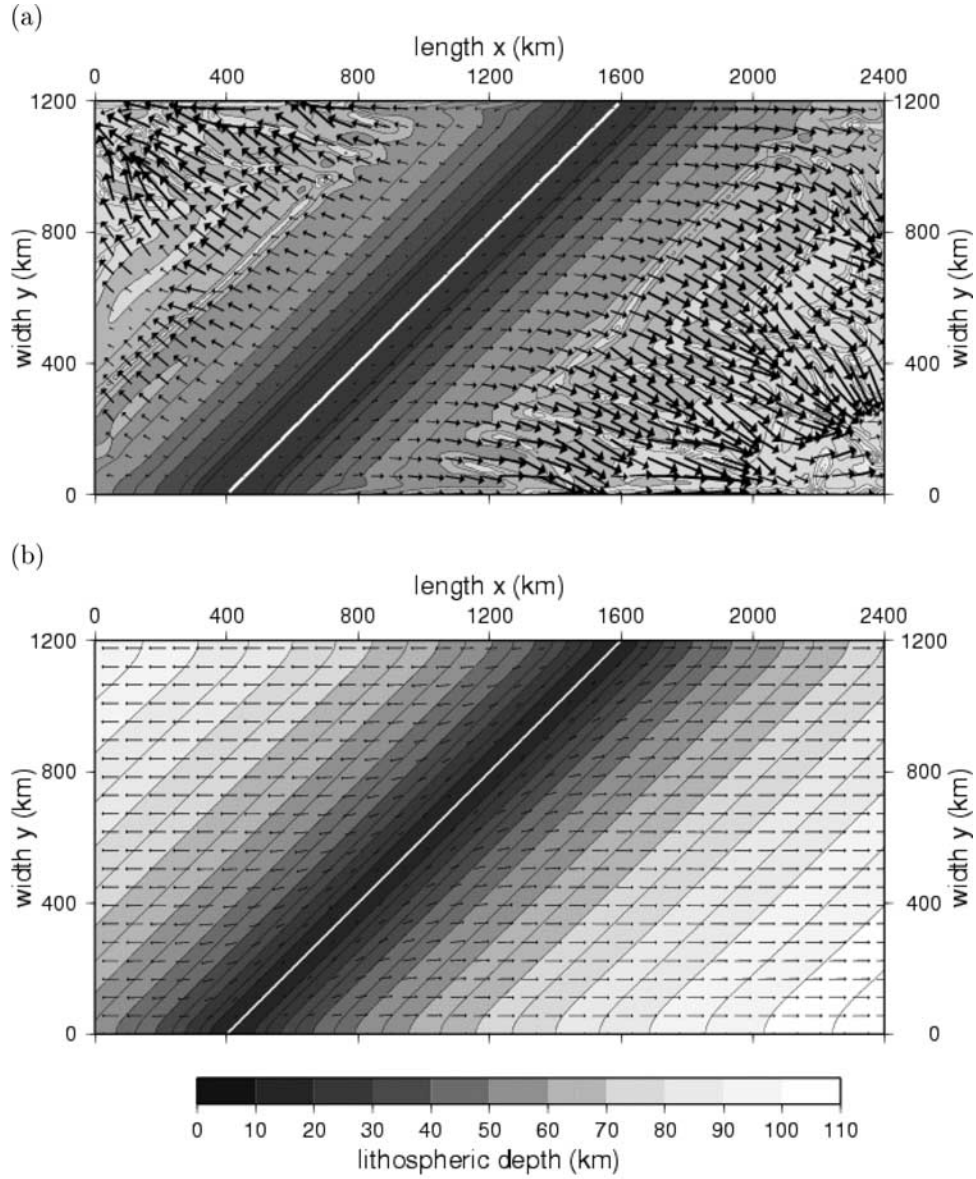

Figure 11. (a) Horizontal velocity field of simulation B at a scaled simulation time of 188 Myr. (b) Horizontal velocity field of a simulation performed in the same conditions but with a null Rayleigh number. Both fields are calculated 100 km below the base of the lithosphere, with u_0 = 2 cm yr^{-1}. The gray scale represents the lithospheric depth, evaluated as the depth of the 1300°C isotherm. Note that for clarity, the velocity scale is different in both cases.

flow in a direction intermediate between plate motion and the direction perpendicular to ridge axis.

5. Ridge Axis With Transform Faults Along the Spreading Center (Case C)

[30] In the following, we will discuss the thermal state and flow obtained at a simulation time of 100 Myr that, in contrast to previous cases, remains later unchanged.

5.1. Flow Description for a Surface Velocity of 2 cm yr^{-1}

[31] This simulation differs from the previous ones by the presence of imposed transform faults. These transform faults separate blocks with different lithospheric ages and therefore generate lateral contrasts in the cooling lithospheric structure. As a result, downgoing instabilities are triggered by the temperature jumps at each transform fault and initiate earlier (16 Ma) than in previous cases (Figure 13a). This agrees with the studies of *Huang et al.* [2003] and of *Dumoulin et al.* [2005]. Finally, mostly due to heat diffusion, temperature jumps across fracture zones, clearly visible at young ages, are wiped out at older ages.

[32] The downgoing instabilities that were, close to the ridge axis, lined up along fracture zones, reorientate in a direction almost perpendicular to the mean ridge axis. Lithospheric topography undulations, if they were frozen within the base of the lithosphere, should be advected with

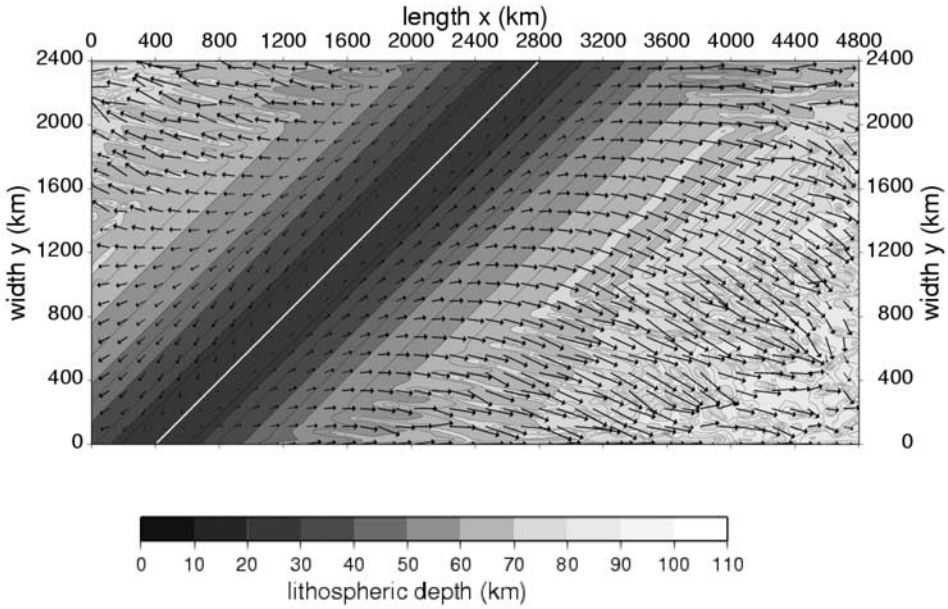

Figure 12. Results of simulation B with $u_0 = 4$ cm yr^{-1}: Horizontal velocity field calculated at 100 km below the base of the lithosphere. The gray scale represents the lithospheric depth, evaluated as the depth of the 1300°C isotherm. This snapshot is taken at a scaled simulation time of 200 Myr.

plate motion, making linear trends. Here, the instabilities progressive rotation means that the undulations are transported toward low y on the right plate and toward large y on the left plate, by the flow within the base of the lithosphere. This flow can be seen on Figure 13a combined to that following the lithospheric topography. The spacing between ridge-perpendicular instabilities is equal to 170 km, corresponding to the spacing between each transform faults along the mean ridge orientation direction (see Figure 1c).

[33] The mantle flow changes to large-scale, 100 km below the base of the lithosphere. It becomes strongly oblique to the plate motion and mostly perpendicular to the mean ridge axis as soon as the instabilities develop (Figure 13b). Figure 13c displays the passive flow induced by plate motion. The passive flow pattern does not show a flow rotation toward the ridge perpendicular direction, nor the increase of velocity 200 km away from the ridge. The buoyancy driven mantle flow (i.e., in excess with respect to the passive flow) therefore parallels the main topographic gradient and is oblique to the applied plate velocity direction.

5.2. Flow Description for a Surface Velocity of 4 cm yr^{-1}

[34] For a surface velocity of 4 cm yr^{-1}, the instability pattern is more complex than in the previous case. As in the case of a 2 cm yr^{-1} surface velocity, downgoing instabilities are triggered by temperature jumps at each transform fault, with an onset time equal to 16 Ma (Figure 14). The youngest downgoing instabilities, marked by a depth increase of the 1300C isotherm on Figure 14, always develop on the old side of transform faults, as observed by [*Huang et al.*, 2003]. These instabilities are, for about 400 km, parallel to the plate motion before reorientating in a direction almost perpendicular to the mean ridge axis. However, in contrast to the previous case, another series of downgoing instabilities initiates at about 27 Ma. These instabilities are first parallel to the plate motion until they join the first "main" series of downgoing instabilities and reorientate almost perpendicularly to mean ridge axis orientation. Further series of instabilities periodically initiates in the gaps formed by the main series, remaining parallel to plate motion until they join the main series.

[35] The spacing between instabilities of the first series is around 340 km, reflecting the spacing between each transform faults in the mean ridge orientation direction. On the other hand, once secondary downgoing instabilities develop, the average instability spacing is equal to around 80 km. The development of a secondary instability is probably due to the imposed distance between the transform faults (240 km), larger in this simulation than in the 2 cm yr^{-1} surface velocity simulation (120 km). The 80 km spacing compares well with that obtained in the same conditions but without fracture zones (see section 3).

[36] As in previous cases, the flow at the base of the lithosphere follows the isotherm topography generated by lithospheric cooling and by downgoing instabilities. The large-scale mantle flow is again parallel to the plate motion close to the ridge axis and becomes later oblique to the plate motion (Figure 14). Downgoing instabilities reorientate along this mantle flow direction.

[37] Surface velocity has an influence on the instability orientation. When it is equal to 2 cm yr^{-1}, downgoing instabilities quickly reorientate almost perpendicularly to the mean ridge axis orientation, despite the plate motion. For a larger surface velocity of 4 cm yr^{-1}, downgoing instabilities generated at transform fault remain longer parallel to the plate motion before reorienting. This can be seen as the result from the competition between the advection of "frozen" instabilities by plate motion and the push exerted by the dynamically driven mantle flow. Further simulations with different surface velocities and fracture

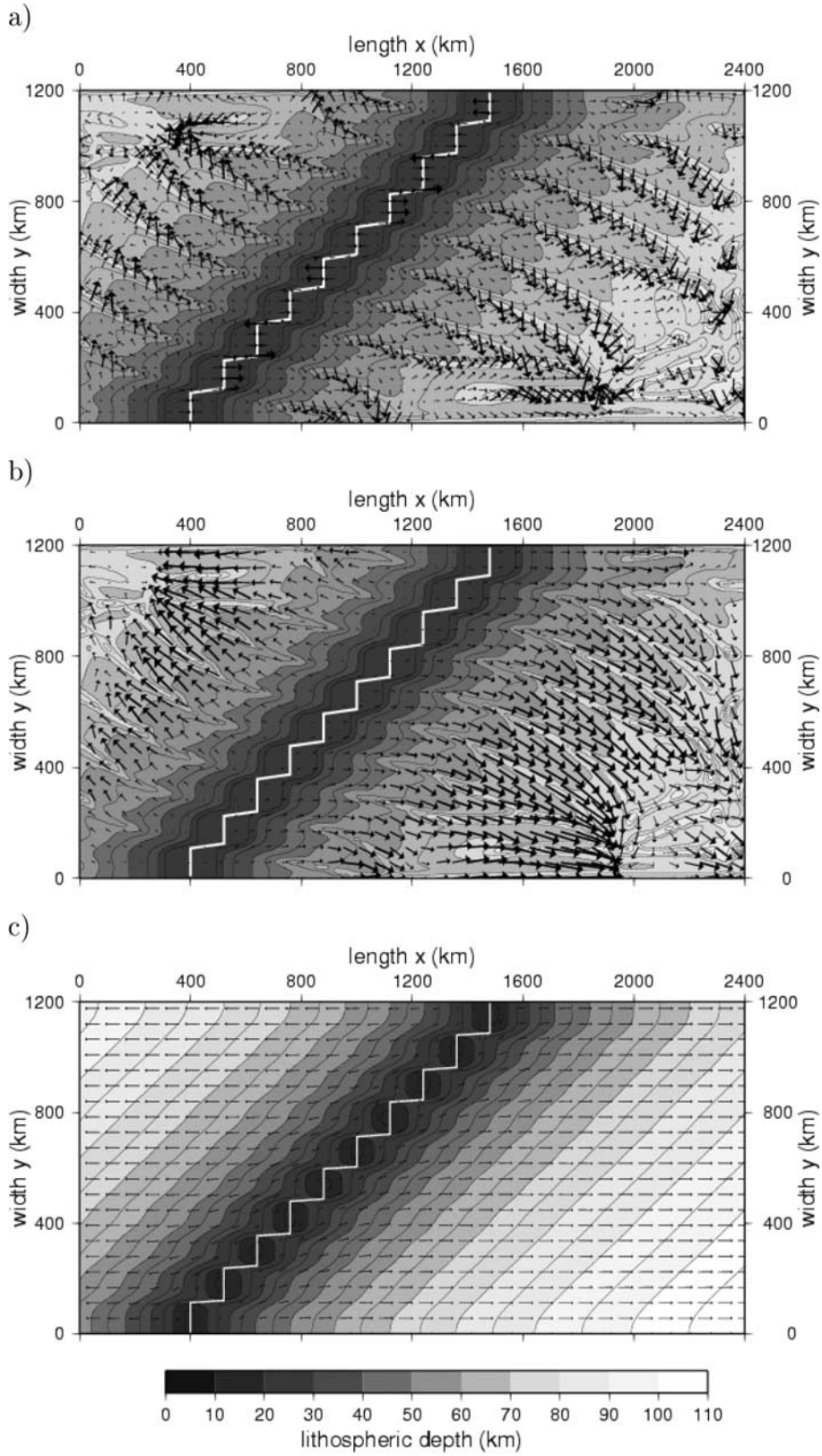

Figure 13. Results of simulation C with $u_0 = 2$ cm yr^{-1}: (a) Horizontal velocity minus the plate velocity of 2 cm yr^{-1} displayed along the base of the lithosphere, (b) total horizontal velocity calculated 100 km below the base of the lithosphere, and (c) total horizontal velocity, calculated 100 km below the base of the lithosphere, of a simulation performed in the same conditions but with a null Rayleigh number. The gray scale represents the lithospheric thickness, evaluated as the depth of the 1300°C isotherm. For clarity, the velocity scale is different in the three cases.

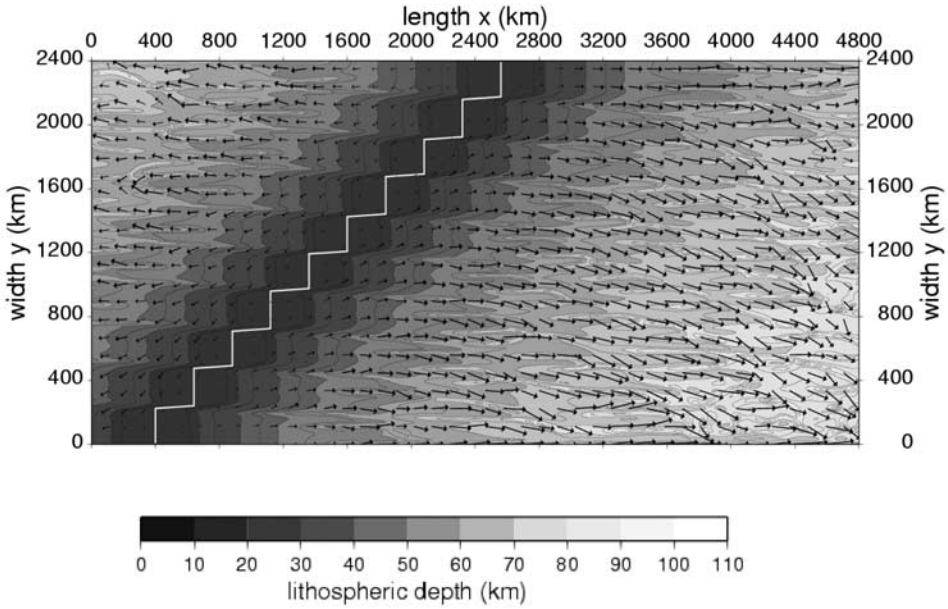

Figure 14. Results of simulation C with u_0 = 4 cm yr^{-1}: Horizontal velocity field calculated 100 km below the base of the lithosphere. The gray scale represents the lithospheric thickness, evaluated as the depth of the 1300°C isotherm.

zones spacing should be performed to better constrain the possible geometry of downgoing instabilities. We expect that the instability orientation will depend on the ratio between the imposed surface velocity (or Peclet number in a nondimensional form) and the asthenospheric viscosity (or Rayleigh number).

6. Discussion

6.1. "Richter's Rolls"

[38] To examine in more details the flow geometry linked to the development of ridge-perpendicular instabilities, we display on Figure 15 a zoom on the temperature, velocity, and velocity rotational fields of case A in a vertical plane perpendicular to the instabilities. We note that SSC, developing mainly at the base of the lithosphere, is superimposed on a large-scale downwelling flow, which brings down the cold drips detaching from the lithosphere until deeper levels in the mantle. This large-scale downward movement, triggered by the drips negative buoyancy, is counterbalanced elsewhere in the box by an upward flow. Secondary convective cells here (as successive clockwise and anticlockwise rolls) present a slight difference to the rolls originally sketched by *Richter and Parsons* [1975] because they are mainly limited to a ~100 km thick layer beneath the lithosphere. This thickness corresponds approximately to the instability spacing, small-scale rolls aspect ratio remaining close to 1. In [*Richter and Parsons*, 1975], the rolls have also an aspect ratio close to 1, but they fill the whole mantle layer, meaning that the mantle layer thickness fixes the rolls spacing.

[39] *Dumoulin et al.* [2005] provided an unscaled relationship of the instability spacing versus $Ra^{-1/3}$ and activation energy. This relationship implies that the instability spacing is controlled by the unstable thermal boundary layer thickness and is independent from the box height. This is also true in our simulations. However, in other experimental setups, the limited depth extent of the asthenosphere may reduce the ability of SSC to form with a spacing larger than the asthenosphere thickness [*Marquart*, 2001; *Huang et al.*, 2003]. For example, in the laboratory experiments of *Vidal* [2004], the SSC spacing depends on the thickness of a "stream jet" impounding beneath the thermal boundary layer, and characterized by a relatively higher temperature and lower viscosity than the surrounding mantle.

6.2. Large-Scale Flow

[40] In all simulations presented above, the flow at the base of the lithosphere relative to plate motion follows the isotherm topography, generated by lithospheric cooling or by downgoing instabilities. This small-scale flow transforms at larger depth to a larger-scale flow (see, for example, Figures 13 and 15). To illustrate this, on Figure 16 we plot different profiles of the horizontal velocity field, u_x, at increasing depths below the lithosphere. Eighty kilometers below the base of the lithosphere, the flow at the scale of the isotherm topography undulations is smoothed out, and presents a pronounced large-scale flow. As soon as the instability develops, the mantle flows in the horizontal direction faster than the plate motion. Note that this forward flow velocity has the same amplitude for both applied plate motions. Close to the ridge, the horizontal velocity decrease with depth reflects the shearing effect induced by plate motion.

[41] The negative buoyancy provided by downwelling thermal instabilities triggers a horizontal large-scale motion, which "on average" goes away from areas without instabilities to areas with well developed instabilities (smoothing out small-scale features). This motion is oriented mainly perpendicularly to the mean ridge axis orientation. This

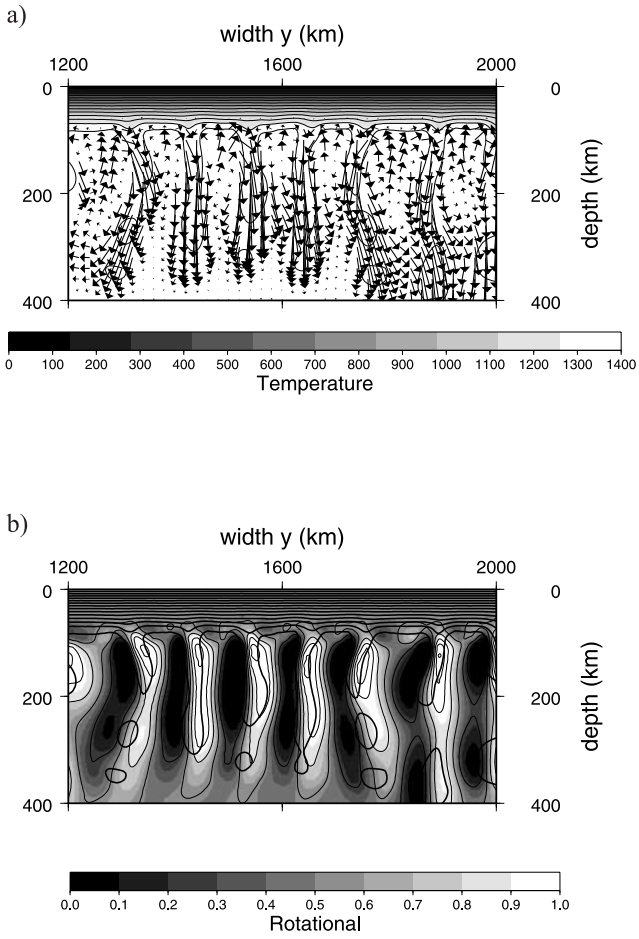

Figure 15. Results of simulation A with u_0 = 4 cm yr^{-1}: Zoom of (a) the temperature and velocity fields and (b) the velocity rotational ($\partial u_z/\partial y - \partial u_y/\partial z$). On Figure 15a, the maximum velocity is equal to 8.30 cm yr^{-1}. On Figure 15b, the rotational is normalized to be bracketed between 0 and 1. Clockwise "cells" and anticlockwise cells are shown by black and white, respectively. The (y, z) vertical cross section is taken at x = 2400 km (as on Figure 9, see location on Figure 8) at a scaled simulation time of 188 Myr.

additional mantle flow, combined with the induced plate motion, results in a flow direction more oblique to plate motion for 2 cm yr^{-1} than for 4 cm yr^{-1} case.

[42] To study whether the large-scale flow and instability orientation depends on the box height and viscosity structure of the upper mantle, another simulation is performed with a strong viscosity increase with depth, a box height of 700 km, and a surface velocity of 2 cm yr^{-1} (other parameters, internal heating, asthenospheric viscosity, etc., are the same as in previous simulations). In this case, the instability and large-scale flow orientation also rotates perpendicularly to the main ridge direction (Figure 17a). Velocities are larger in the asthenosphere than deeper in the mantle (Figure 17b). In contrast to previous simulations, (for comparison, see Figures 6a and 6c), the depth and lateral extents of the large-scale flow cells are limited by the high viscosity bottom layer (2.7×10^{21} Pa s) that acts as flow barrier with little "permeability." Therefore the large-scale flow induced by the negative buoyancy provided by the lithospheric sublayer instabilities, is not, in this simulation, exaggerated by the bottom open boundary condition.

6.3. Simple Shear Orientation Quantification

[43] Seismic anisotropy can be used to probe the mantle flow pattern beneath the oceanic lithosphere, since it results from olivine lattice-preferred orientation (LPO) produced by mantle deformation. However, recent studies show that anisotropy does not simply relate to the flow pattern [*Tommasi*, 1998; *Kaminski and Ribe*, 2002]. These authors propose that, at small strain, the mean a axis orientation (olivine fast axis) aligns itself with the longest axis of the finite strain ellipsoid. However, at large strain and in the case of a simple shear flow, the mean a axis orientation no longer follows the finite strain ellipsoid but rotates toward

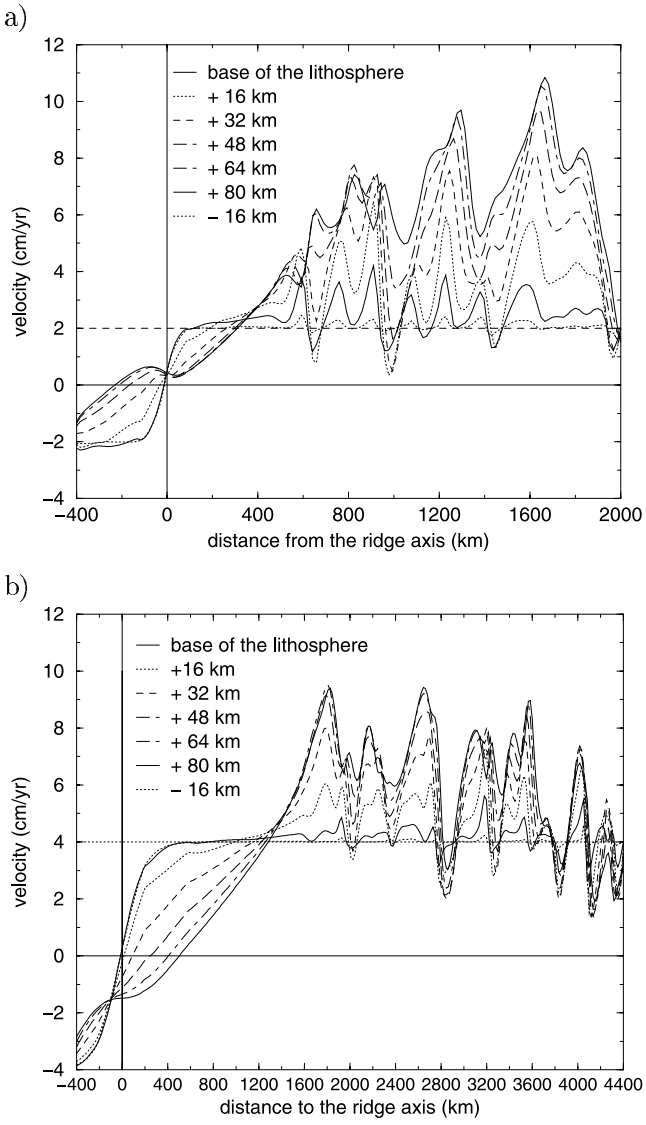

Figure 16. Horizontal velocities, u_x, at different depth locations compared to the base of the lithosphere in the case of a linear ridge perpendicular to the plate motion (case A). Profiles are taken at y = 600 and 1200 km for surface velocities of (a) 2 cm yr^{-1} and (b) 4 cm yr^{-1}, respectively. Simulation time is of 190 Myr.

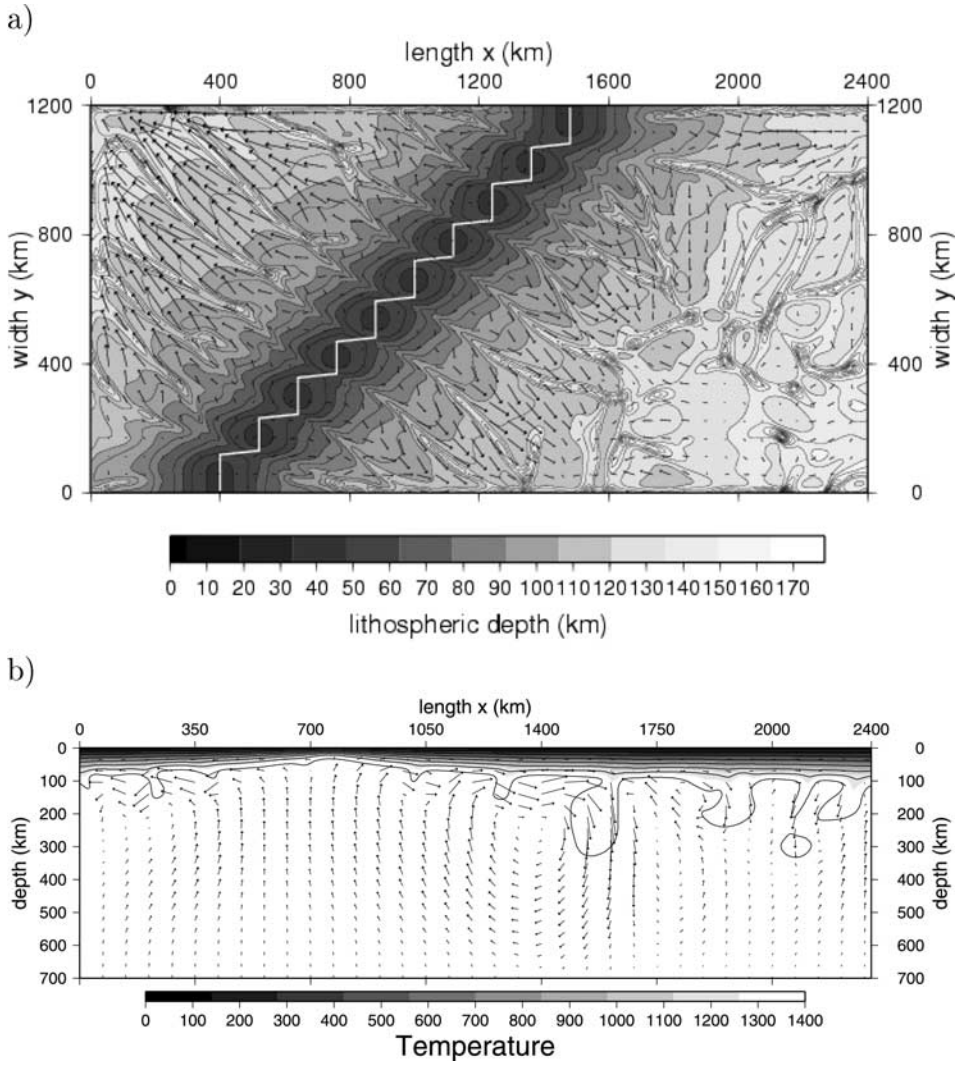

Figure 17. Results of a simulation performed with a box height of 700 km and u_0 = 2 cm yr^{-1}. The viscosity increases with depth of a factor 100 at 250 km depth. In this case, $Ra = 2.22 \times 10^8$ (based on the same asthenospheric viscosity as in previous simulations). (a) Horizontal velocity calculated 100 km below the base of the lithosphere (the gray scale represents the lithospheric thickness). (b) Temperature and velocity fields displayed on a vertical plane located at y = 400 km.

the simple shear direction due to dynamic recrystallization [*Zhang et al.*, 2000; *Kaminski and Ribe*, 2002].

[44] Thus, in order to obtain a very crude quantification of the anisotropy orientation generated by the modeled mantle flow, we evaluate the average horizontal shear ($\partial u_{horizontal}/\partial z$) direction, θ. As the angle θ varies spatially on a scale smaller than the anisotropy resolution in surface wave tomographic models, on Figure 18 we represent a distribution of θ, at three distances from the ridge axis (different lithospheric ages) and at two different depths. Note that the plate motion orientation corresponds to θ equal to 90°. The perpendicular to the mean ridge is orientated either at 90° (case A) or at 135° (cases B and C). The θ angle distribution is obtained from the θ value calculated at each model node on model surface portions located at a distance of 600 ± 167 km, 892 ± 167 km, and 1192 ± 167 km from the ridge axis for u_0 = 2 cm yr^{-1} (and at 1592 ± 167 km, 2025 ± 167 km, and 2792 ± 167 km for u_0 = 4 cm yr^{-1}). These locations correspond to lithospheric ages of 30, 60, and 84 Ma (36, 64, and 72 Ma, respectively). To limit the influence of the box side boundaries, we exclude from the distribution estimate the nodes closer than 233 km (483 km, respectively) from the box front and back sides. The horizontal shear distributions are calculated either at the base of the lithosphere (along the 1300°C isotherm) or 145 km below the base of the lithosphere.

[45] The shear orientation direction at the base of the lithosphere (solid bars on Figure 18) depends on the geometry of the base of the lithosphere (either inherited or developing through boundary layer instabilities). For a linear ridge perpendicular (case A) or oblique (case B) to plate motion, it is mainly oriented at 90° (case A) or at 135° (case B), before the instability onset or as long as ridge-parallel instabilities develop. In cases A and B, as soon as ridge-perpendicular instability develop, the θ distribution becomes fuzzier, with no clear dominant orientation, show-

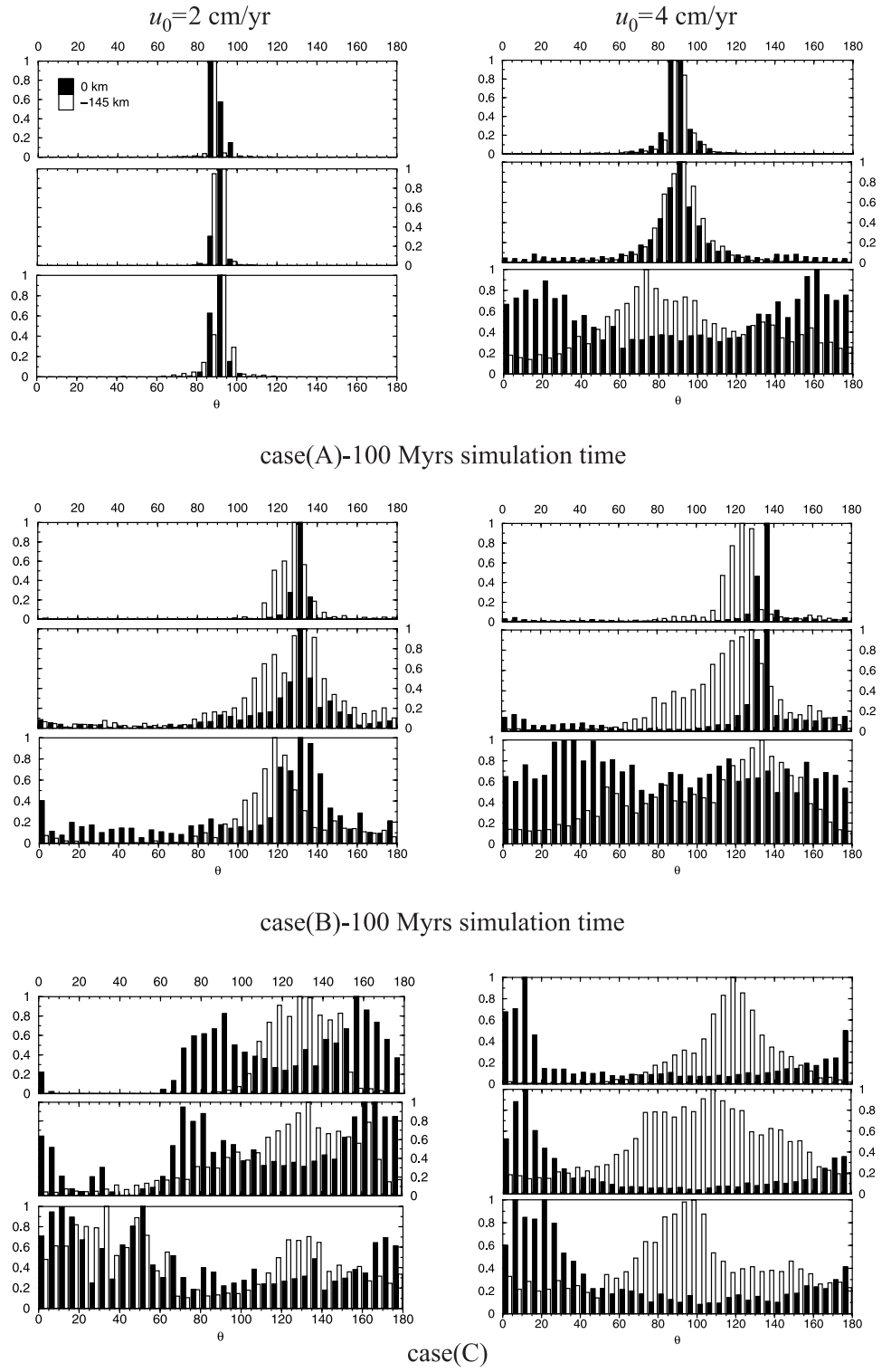

Figure 18. Distribution of the horizontal simple shear direction ($\partial u_{horizontal}/\partial z$) for the three ridge geometry cases (A, B,and C) and for the two imposed plate velocities (u_0 = 2 and 4 cm yr^{-1}). The plate motion orientation corresponds to θ = 90°. The horizontal simple shear direction is evaluated at the base of the lithosphere (isotherm 1300°C) or at 145 km below the base of the lithosphere at three distances from the ridge axis (from top to bottom), 600, 892, and 1192 km (1592, 2025, and 2792 km) for u_0 = 2 cm yr^{-1} (u_0 = 4 cm yr^{-1}, respectively).

ing a competition between a mantle shearing effect and the convergent movement toward lithospheric undulations.

[46] The shear orientations (around 90° and 160°) at the base of the lithosphere, for a ridge separated by transform faults (case C) and a surface velocity of 2 cm yr^{-1}, reflects the combination between the convergent flow stepping down topographic lineations, and the flow responsible for the lineation reorientation (see Figure 13a and section 5.1). For a surface velocity of 4 cm yr^{-1}, the shear is oriented mainly around 0–20°, i.e., perpendicular to the instability lineations (Figure 14).

[47] The shear flow scale and orientation progressively change with depth. At 145 km below the base of the lithosphere, the shear orientation characterizes the large-scale mantle flow. It is more homogeneous than the shear orientation at the base of the lithosphere. Shear is aligned with plate motion for case A ($\theta \sim 90°$) and is oblique to plate motion for cases B and C ($\theta \sim 130°$ for cases B and C, u_0 = 2 cm yr^{-1}, and $\theta \sim 100–125°$ for case C, u_0 = 4 cm yr^{-1}). The large-scale mantle shear is therefore oriented in a direction intermediate between the perpendicular to the mean ridge orientation and the plate motion. We suspect that this obliquity to plate motion depends on the ratio between the plate velocity and the large-scale mantle flow generated by the negative buoyancy of small-scale instabilities.

[48] We conclude that surface wave tomography in the uppermost mantle should average small-scale, possibly complex, features associated to the geometry of the developing thermal boundary layer instabilities, plus a large-scale pattern that derives from a combination between shearing induced by plate motion and an internally driven flow. Tomographic models including azimuthal anisotropy show a fast seismic velocity orientation globally perpendicular to the mean ridge orientation and often oblique to plate motion [e.g., *Montagner*, 2002; *Debayle and Sambridge*, 2004]. A possible explanation for this obliquity is the presence of a large-scale forward mantle flow, internally driven by the negative buoyancy of thermal boundary layer instabilities developing at the base of the lithosphere. Low anisotropy zones observed at some distance from the ridge axis (between 40 and 60 Ma) down to 200 km depth below the Pacific plate [*Montagner*, 2002] or below the Indian Ocean [*Lévêque et al.*, 1998] may also be related to the SSC onset.

6.4. Boundary Condition Effects

[49] In cases A and B, ridge-perpendicular instabilities aligned with the main mantle shear direction are favored by the free slip boundary conditions applied on the box front and back sides. Because of the shear flow, these instabilities are intrinsically more stable than ridge-parallel ones. However, the growth of thermal boundary layer instabilities is also strongly sensitive to the perturbation pattern (see *Dumoulin et al.* [2005] for a discussion). In our simulations, perturbations arise either from the neighboring inherited lithospheric thermal structure, or from small amplitude thermal fluctuations in the core flow. Here, the vanishing tangential stresses imposed on the box front and back sides strongly promote the formation of downgoing instabilities along these sides (Figure 8). These instabilities enhance the growth of neighboring instabilities in a direction as parallel as possible from the box side (Figure 11). Step by step, they orientate along the shear direction and form a V shape that reflects the competition with the development of ridge-parallel instabilities. In a similar way, inherited thermal structure as transform faults (case C) will also influence the orientation of lineations growing next to them (Figure 13). The competing influence of ridge-parallel instabilities and of upstream and neighboring lithospheric structures may produce transient states (here, for cases A and B). The latter are, in general, intrinsically less relevant for the Earth than the final steady state flow pattern, but it might not be always the case, especially for simulations where boundary conditions strongly influence the final geometry.

[50] An additional boundary condition effect appears in cases B and C, where the large-scale flow is, on average, oblique to the plate motion. The closed front and back sides of the box then appear as a main flow barrier. However, opening these sides would also have created artefacts, although more subtle, as the assumed open boundary symmetry (either on normal stress or on velocity) would still not fit with the large-scale flow geometry. Therefore we focus on the large-scale flow geometry far away from these sides.

6.5. Earth Scaling

[51] In our simulations, the imposed surface velocity influences downgoing instability and large-scale flow final orientations. Note that our parameter choice results in a Peclet number (nondimensional surface velocity) over Rayleigh number ratio that is relatively low compared to that of other studies [e.g., *van Hunen et al.*, 2003]. Consequently, the tangential force exerted by the mantle flow at the base of the lithosphere is, in the cases presented here, mainly controlled by internally driven convective mantle processes and not by the relative shearing imposed by the moving plate, as shown by *Lux et al.* [1979]. On the contrary, the shearing imposed by plate motion eliminates ridge-parallel instabilities for the benefit of ridge-perpendicular ones in the study of *van Hunen et al.* [2003]. One may thus ask for the validity of our parameter choices. The difficulty is that we do not know a priori what is the Peclet over Rayleigh numbers ratio in the Earth. Models including self-consistently the generation of plate tectonics do not yet help us, because plate motions then strongly depend on the employed rheology at plate boundaries [e.g., *Tackley*, 2000a, 2000b].

[52] One way to scale numerical simulations is to insure that the heat flow supplied by SSC in simulations is close to that provided at the base of the Earth's oceanic lithosphere. This heat flow is constrained by geophysical observations, as the subsidence of seafloor topography, the surface heat flow at old ages, and the geoid [*Stein and Stein*, 1992; *Doin and Fleitout*, 2000]. Alternatively, the scaling could be based on the assumption that the SSC onset age is, say, ~70 Ma. However, in contrast to the relatively tight constraints on the mantle heat flow, conductive models applied to the cooling of the oceanic lithosphere are compatible with a wide range of SSC onset times (from 0 to 80 Ma [*Doin and Fleitout*, 1996]). Therefore we scale the box height in our simulations in order to obtain an heat flow provided by SSC of about 40 mW m^{-2}, and an equilibrium lithospheric thickness of ~100 km (see Figure 4, note that at 100 Ma,

the lithosphere is still cooling due to the delay introduced by conduction in the lid and by the early SSC onset). For a Rayleigh number of 4.2×10^7 and other parameters defined in Table 1, our box height choice corresponds to setting the mantle viscosity to 2.7×10^{18} Pa s. It is in agreement with the viscosity derived from heat flow scaling laws obtained by *Davaille and Jaupart* [1994], *Dumoulin et al.* [1999], and *Solomatov and Moresi* [2000]. Such a low viscosity also agrees with dynamic modeling using geoid, topography, and plate velocity [*Cadek and Fleitout*, 1999].

[53] Our simulations scaling results in a spacing between ridge-parallel and ridge-perpendicular instabilities ranging from 145 to 175 km, and from 80 to 145 km, respectively, in good agreement with obtained scaling law [*Dumoulin et al.*, 2005]. This order of magnitude is at the lower range of short-wavelength undulations reported by *Haxby and Weissel* [1986], ranging from 150 to 500 km. However, note that the scaling law obtained for instability spacing shows that it does not depend on the simulation box height but mostly on the asthenospheric viscosity and activation energy [*Dumoulin et al.*, 2005]. Therefore choosing a larger asthenospheric viscosity should result in a larger instability spacing. Similarly, the scaled SSC onset ages (30–40 Ma for smooth ridges, 16 Ma with transform faults) would have been larger if scaled with a larger asthenospheric viscosity (see *Huang et al.* [2003] and *Dumoulin et al.* [2005] for more discussion).

7. Conclusion

[54] The ridge geometry has a strong influence on the orientation of thermal boundary layer instabilities and on the mantle flow pattern. In the case of a linear ridge axis perpendicular or oblique to the plate motion direction (cases A and B), we first observe a series of downgoing instabilities parallel to the ridge axis at young ages, developing at 30–40 Ma. This geometry shows that the base of the lithosphere becomes unstable at a uniform age along the ridge direction. These instabilities are then advected with plate motion until they are destroyed by the growth of ridge-perpendicular instabilities. The latter are intrinsically more stable because they are lined up with the mantle shear direction.

[55] In the case of a ridge separated by transform faults (case C), instabilities initiate at each transform fault, twice earlier (16 Ma) than in previous cases. First aligned with the transform faults, they later rotate perpendicularly to the mean ridge axis. If the transform fault spacing is large enough, other series of downgoing instabilities are generated later, in the gaps between fracture zones. They are first parallel to the plate motion until they join ridge-perpendicular instabilities. The jump in thermal structure between lithospheric blocks separated by transform faults is quickly smoothed out by the SSC effect.

[56] In all cases, the flow that occurs at a small scale at the base of the lithosphere transforms to a large-scale pattern deeper in the mantle. This large-scale flow is a combination of the mantle shear flow entrained by the imposed plate velocity and a forward flow, internally driven by the negative buoyancy of thermal boundary layer instabilities. This additional large-scale flow is mainly horizontal and strongly controlled by the mean ridge axis orientation. It may thus be oblique to the imposed plate motion direction. The final large-scale flow orientation should therefore result from the relative amplitude of plate motion and internally driven mantle flow. The azimuthal anisotropy modeled by surface wave tomography shows that fast seismic velocity axes are mostly perpendicular to the average ridge orientation. This could be explained by the presence of a nonnegligible large-scale mantle forward flow driven by the growth of small-scale instabilities beneath the oceanic lithosphere.

[57] **Acknowledgment.** We wish to thank the Associate Editor Shijie Zhong and Jeoren van Hunen for their helpful comments on the manuscript.

References

Albers, M. (2000), A local mesh refinement multigrid method for 3-D convection problems with strongly variable viscosity, *J. Comput. Phys.*, *160*, 126–150.

Becker, T. W., J. B. Kellogg, G. Ekström, and R. J. O'Connell (2003), Comparison of azimuthal seismic anisotropy from surface waves and finite strain from global mantle-circulation models, *Geophys. J. Int.*, *155*, 696–714.

Blankenbach, B., et al. (1989), A benchmark comparison for mantle convection codes, *Geophys. J. Int.*, *98*, 23–38.

Buck, W. R., and E. M. Parmentier (1986), Convection beneath young oceanic lithosphere: Implications for thermal structure and gravity, *J. Geophys. Res.*, *91*, 1961–1974.

Busse, F. H., et al. (1993), 3D convection at infinite Prandtl number in Cartesian geometry—A benchmark comparison, *Geophys. Astrophys. Fluid Dyn.*, *75*, 39–59.

Cadek, O., and L. Fleitout (1999), A global geoid model with imposed plate velocities and partial layering, *J. Geophys. Res.*, *104*, 29,055–29,075.

Cazenave, A., B. Lago, and K. Dominh (1983), Thermal parameters of the oceanic lithosphere estimated from geoid height data, *J. Geophys. Res.*, *88*, 1105–1118.

Christensen, U., and H. Harder (1991), 3D convection with variable viscosity, *Geophys. J. Int.*, *104*, 213–226.

Davaille, A., and C. Jaupart (1993), Transient high-rayleigh-number thermal convection with large viscosity variations, *J. Fluid Mech.*, *253*, 141–166.

Davaille, A., and C. Jaupart (1994), Onset of thermal convection in fluids with temperature-dependent viscosity: Application to the oceanic mantle, *J. Geophys. Res.*, *99*, 19,853–19,866.

Debayle, E., and M. Sambridge (2004), Inversion of massive surface wave data sets: Model construction and resolution assessment, *J. Geophys. Res.*, *109*, B02316, doi:10.1029/2003JB002652.

Doin, M. P., and L. Fleitout (1996), Thermal evolution of the oceanic lithosphere: An alternative view, *Earth Planet. Sci. Lett.*, *142*, 121–136.

Doin, M. P., and L. Fleitout (2000), Flattening of the oceanic topography and geoid: thermal versus dynamic origin, *Geophys. J. Int.*, *143*, 582–594.

Driscoll, M. L., and B. Parsons (1988), Cooling of the oceanic lithosphere-evidence from geoid anomalies across the Udintsev and Eltanin fracture zones, *Earth Planet. Sci. Lett.*, *88*, 289–307.

Dumoulin, C., M.-P. Doin, and L. Fleitout (1999), Heat transport in stagnant lid convection with temperature- and pressure-dependent Newtonian or non-Newtonian rheology, *J. Geophys. Res.*, *104*, 12,759–12,778.

Dumoulin, C., M.-P. Doin, and L. Fleitout (2001), Numerical simulations of the cooling of an oceanic lithosphere above a convective mantle, *Phys. Earth Planet. Inter.*, *125*, 45–64.

Dumoulin, C., M.-P. Doin, D. Arcay, and L. Fleitout (2005), Onset of small-scale instabilities at the base of the lithosphere: Scaling laws and role of pre-existing lithospheric structures, *Geophys. J. Int.*, *160*(1), 345–357, doi:10.1111/j.1365-246X.2004.02475.x.

Ekström, G., and A. M. Dziewonski (1998), The unique anisotropy of the Pacific upper mantle, *Nature*, *394*, 168–172.

Freedman, A. P., and B. Parsons (1990), Geoid anomalies over two South Atlantic fracture zones, *Earth Planet. Sci. Lett.*, *100*, 18–41.

Haxby, W. F., and J. K. Weissel (1986), Evidence for small-scale mantle convection from Seasat altimater data, *J. Geophys. Res.*, *91*, 3507–3520.

Huang, J., S. Zhong, and J. van Hunen (2003), Controls on sublithospheric small-scale convection, *J. Geophys. Res.*, *108*(B8), 2405, doi:10.1029/2003JB002456.

Kaminski, É., and N. M. Ribe (2002), Timescales for the evolution of seismic anisotropy in mantle flow, *Geochem. Geophys. Geosyst.*, *3*(8), 1051, doi:10.1029/2001GC000222.

Korenaga, J., and T. H. Jordan (2003), Physics of multiscale convection in Earth's mantle: Onset of sublithospheric convection, *J. Geophys. Res.*, *108*(B7), 2333, doi:10.1029/2002JB001760.

Lévêque, J. J., E. Debayle, and V. Maupin (1998), Anisotropy in the Indian Ocean upper mantle from Rayleigh- and Love-waveform inversion, *Geophys. J. Int.*, *133*, 529–540.

Lux, R. A., G. F. Davies, and J. H. Thomas (1979), Moving lithospheric plates and mantle convection, *Geophys. J. R. Astron. Soc.*, *58*, 209–228.

Marquart, G. (2001), On the geometry of mantle flow beneath drifting lithospheric plates, *Geophys. J. Int.*, *144*, 356–372.

Montagner, J.-P. (2002), Upper mantle low anisotropy channels below the Pacific Plate, *Earth Planet. Sci. Lett.*, *202*, 263–274.

Morgan, J. P., and E. M. Parmentier (1995), Crenulated seafloor: Evidence for spreading-rate dependent structure of mantle upwelling and melting beneath a mid-oceanic spreading center, *Earth Planet. Sci. Lett.*, *129*, 73–84.

Morris, S., and D. Canright (1984), A boundary-layer analysis of Benard convection in a fluid of strongly temperature-dependent viscosity, *Phys. Earth Planet. Inter.*, *36*, 355–373.

Parsons, B., and D. McKenzie (1978), Mantle convection and the thermal structure of the plates, *J. Geophys. Res.*, *83*, 4485–4496.

Parsons, B., and J. G. Sclater (1977), An analysis of the variation of ocean floor bathymetry and heat flow with age, *J. Geophys. Res.*, *82*, 803–827.

Rabinowicz, M., S. Rouzo, J. C. Sempéré, and C. Rosenberg (1993), Three-dimensional mantle flow beneath mid-ocean ridges, *J. Geophys. Res.*, *98*, 7851–7869.

Richter, F. M. (1973), Convection and the large-scale circulation of the mantle, *J. Geophys. Res.*, *78*, 8735–8745.

Richter, F. M., and B. Parsons (1975), On the interaction of two scales of mantle convection, *J. Geophys. Res.*, *80*, 2529–2541.

Ritzwoller, M. H., N. M. Shapiro, and S.-J. Zhong (2004), Cooling history of the Pacific lithosphere, *Earth Planet. Sci. Lett.*, *226*, 69–84.

Sandwell, D. T., and G. Schubert (1982), Geoid height-age relation from Seasat altimeter profiles across the Mendocino fracture zone, *J. Geophys. Res.*, *87*, 3949–3958.

Solomatov, V. S., and L. N. Moresi (2000), Scaling of time-dependent stagnant lid convection: Application to small-scale convection on Earth and other terrestrial planets, *J. Geophys. Res.*, *105*, 21,795–21,817.

Stein, C. A., and S. Stein (1992), A model for the global variation in oceanic depth and heat flow with lithospheric age, *Nature*, *359*, 123–129.

Tackley, P. J. (1993), Effects of strongly temperature dependent viscosity on time-dependent, three-dimensional models of mantle convection, *Geophys. Res. Lett.*, *20*, 2187–2190.

Tackley, P. J. (2000a), Self-consistent generation of tectonic plates in time-dependent, three-dimensional mantle convection simulations: 1. Pseudo-plastic yielding, *Geochem. Geophys. Geosyst.*, *1*(8), doi:10.1029/2000GC000036.

Tackley, P. J. (2000b), Self-consistent generation of tectonic plates in time-dependent, three-dimensional mantle convection simulations, 2. Strain weakening and asthenosphere, *Geochem. Geophys. Geosyst.*, *1*(8), doi:10.1029/2000GC000043.

Tommasi, A. (1998), Forward modeling of the development of seismic anisotropy in the upper mantle, *Earth Planet. Sci. Lett.*, *160*, 1–13.

Turcotte, D. L., and E. R. Oxburgh (1967), Finite amplitude convective cells and continental drifts, *J. Fluid Mech.*, *28*, 29–42.

van Hunen, J., J. Huang, and S. Zhong (2003), The effect of shearing on the onset and vigor of small-scale convection in a Newtonian rheology, *Geophys. Res. Lett.*, *30*(19), 1991, doi:10.1029/2003GL018101.

Vidal, V. (2004), Interaction des differentes échelles de convection dans le manteau terrestre, Ph.D. thesis, Inst. de Phys. du Globe de Paris, Paris.

Zhang, S., S. Karato, J. F. Gerald, U. H. Faul, and Y. Zhou (2000), Simple shear deformation of olivine aggregates, *Tectonophysics*, *316*, 133–152.

M.-P. Doin, Ecole Normale Supérieure, Laboratoire de Géologie, 24 rue Lhomond, F-75231 Paris Cedex 05, France.

C. Dumoulin, Laboratoire de Planétologie et Géodynamique, Université de Nantes, 2 rue de la Houssinière, B.P. 92208, F-44322 Nantes Cedex 3, France.

C. Morency, Department of Oceanography, Dalhousie University, Halifax, NS, Canada B3H 4J1. (christina.morency@dal.ca)